AGU PUBLICATIONS

Water Resources Research

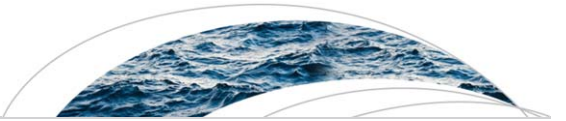

RESEARCH ARTICLE

10.1002/2017WR021302

Fluid Topology in Pore Scale Two-Phase Flow Imaged by Synchrotron X-ray Microtomography

Hamid Hosseinzade Khanamiri[1] and **Ole Torsæter**[1]

[1]Department of Geoscience and Petroleum, PoreLab Research Center, Norwegian University of Science and Technology, Trondheim, Norway

Key Points:
- Time-resolved study of pore scale fluid topology in two-phase flow was performed by synchrotron X-ray computed microtomography
- $\chi - Sw$ profiles showed hysteresis in drainage and imbibition for a fluid phase and its ganglia, while little or no hysteresis for connected pathway
- The ganglia contributed to flow by creating internal redundant connections, volume exchange with connected pathway and saturation change

Supporting Information:
- Supporting Information S1

Correspondence to:
H. H. Khanamiri,
hamid.hosseinzade@ntnu.no

Citation:
Khanamiri, H. H., & Torsæter, O. (2018). Fluid topology in pore scale two-phase flow imaged by synchrotron X-ray microtomography. *Water Resources Research*, *54*, 1905–1917. https://doi.org/10.1002/2017WR021302

Received 12 JUN 2017
Accepted 24 FEB 2018
Accepted article online 28 FEB 2018
Published online 15 MAR 2018

The copyright line for this article was changed on 10 DEC 2018 after original online publication.

Abstract A flow experiment including drainage and imbibition by water and surfactant was performed on a water-wet Berea sandstone. The three-dimensional (3-D) pore scale changes of the fluid configuration were captured under flow using synchrotron X-ray computed microtomography. Euler characteristic of ganglia and connected pathway was calculated to study topology of these entities. In addition, Betti numbers and volumes of the ganglia and connected pathway were calculated to study their contribution in the flow. Results showed that Euler characteristic of the ganglia and the whole phase (ganglia plus connected pathway) versus saturation exhibited hysteresis in imbibition and drainage. However, the Euler characteristic of the connected pathway versus saturation had insignificant hysteresis in imbibition and drainage. Results of the Betti numbers and volume changes in nonwetting ganglia and connected pathway showed that the ganglia contributed to the flow by creating internal redundant connections, volume exchange with the connected pathway and saturation change. Further, the number of redundant connections in nonwetting connected pathway increased in drainage and decreased in imbibition, smoothly in both cases, with insignificant sensitivity to the changes in rate and interfacial tension.

1. Introduction

The fundamentals of two-phase flow in porous media have been partly unknown due to limitations in studying the dynamics. The associated ambiguity has also hindered the efforts for upscaling the microscopic changes to larger scale in industry applications including but not limited to enhanced oil recovery (EOR), CO_2 sequestration, and groundwater. Darcy scale (Brown, 2002; Darcy, 1856) coreflooding has been a major method in the research and the routine industrial experiments of two-phase flow. It is necessary and informative. Nevertheless, in such an experiment only a number of macroscopic properties are measured, with limited direct evidence on the governing microscopic changes. Pore scale imaging by X-ray computed microtomography has the potential to reconstruct the internal structure of the porous rocks to visualize and to quantify the outcome of a flow process. Digital core analysis using X-ray imaging has recently become a routine task in oil and gas laboratories (Blunt et al., 2013). Although the image processing in microtomography involves challenging steps of noise filtering and phase segmentation which can be user-biased (Leu et al., 2014), the X-ray microtomography gives the distribution and size of oil clusters inside the pores. Thus, it becomes feasible to study the unknown phenomena, which are invisible in ordinary core flooding experiments. However, a single scan to resolve the pore scale configuration of oil and water or even a dry porous media can take several hours in an ordinary micro-CT machine depending on the spatial resolution. Therefore, only the initial and final conditions of a flow test can be imaged.

The dynamics of flow can be captured in the micromodel experiments. The earlier two-dimensional (2-D) studies mainly on the etched glass micromodels or the modeling of such systems showed that the nonwetting fluid moved either as a connected pathway or as a group of disconnected clusters (ganglia) which broke up and coalesced (Avraam & Payatakes, 1995). The phenomenon where the disconnected clusters of the nonwetting phase are mobile is known as the ganglion dynamics. It has also been observed that a real 3-D porous system can represent a different behavior than a 2-D system. Avraam et al. (1994) used planar 2-D models and nonplanar 3-D models to study the impact of the nonplanarity in the observed flow mechanisms. They concluded that nonplanarity had small qualitative but significant quantitative effect in the ganglion size distribution and the mean ganglion size under the same flow conditions.

The dynamics in a 3-D porous media can be captured by the synchrotron X-ray tomography where the temporal resolution is in the order of minutes and seconds. Synchrotron imaging has helped to understand better behavior of flowing fluids. Youssef et al. (2014) found that mean ganglia size and largest cluster size depended on capillary number. Armstrong et al. (2014) modified the traditional capillary number by incorporating the nonwetting phase cluster length. Having observed the dynamics of flow, they said that desaturation by an increase in flow rate or viscosity or decrease in interfacial tension were different. Rücker et al. (2015) observed that ganglion dynamics occurred at a length scale similar to oil clusters length. Therefore, an intermediate flow regime between pore and Darcy scales was expected. Berg et al. (2015) showed that at the onset of oil mobilization, oil clusters broke off as opposed to moving in the form of a single large cluster. They reported that the clusters broke off further into smaller segments while in only fewer occasions the clusters merged. Pak et al. (2015) reported also that the nonwetting phase droplets were fragmented when trapped at large pores of a highly heterogeneous carbonate rock under imbibition for both high and low capillary numbers. They performed the experiment using ordinary X-ray microtomography. Singh et al. (2017b) reported two different fluid patterns in wettability-controlled experiments. They observed a compact front morphology in imbibition and a fingered morphology in drainage. In another work, Singh et al. (2017a) showed that wetting-nonwetting interface movement and brine layer swelling, responsible for snap-off phenomenon, took place in several minutes. This is orders of magnitude slower than the time scale of Haines jumps (Haines, 1930) in drainage. Armstrong et al. (2016) found that the Darcy description of the two-phase flow originated from the connected pathway flow and the dissipative pore-scale events due to the oil-water interface jumps. They observed that these two flow regimes coexisted during fractional flow. They also mapped the contribution of each flow regime in a phase diagram representing the flux of each flow regime at varying capillary numbers and saturations.

One of the major challenges has been to find a parameter which helps quantifying the dynamic microscopic changes. In this regards, Herring et al. (2013) used Euler characteristic (χ) to describe the connectivity of the oil clusters. This parameter was previously used as a descriptor of porous structures to characterize the connectivity (Mecke & Arns, 2005). Euler characteristic (χ) is defined as:

$$\chi = \frac{M_3}{4\pi} = \beta_0 - \beta_1 + \beta_2. \tag{1}$$

In this equation, $\beta_0 - \beta_2$ are the Betti numbers. The zeroth Betti number, β_0, is the number of isolated clusters of a fluid phase, the first Betti number, β_1, is the number of redundant connections within all clusters, and the second Betti number, β_2, is the number of cavities or hollows, e.g., a water drop inside an oil drop. The number of redundant connections in a 3-D object is the number of connections, which can be cut in a manner that the object is not divided into two or more. A negative value of χ indicates higher connectivity while a positive value indicates fragmented fluid. The Euler characteristic is also known as the integrated Gaussian curvature (M_3), which is one of the four Minkowski functionals with M_0 the volume, M_1 the surface area, and M_2 the integrated mean curvature. According to Hadwiger's characterization theorem in integral geometry (Hadwiger, 1957), any continuous function that is invariant under rigid motion can be written as a linear combination of the Minkowski functionals. In three dimensions, there is $3 + 1$ such functions (M_0–M_3), as mentioned above. The Euler characteristic (χ) is dimensionless; however, it is usually normalized with the total volume of the system (the bulk volume) for convenience. In this work, we have reported the normalized values in mm^{-3} unit. Schlüter et al. (2016) believed that the wetting phase saturation, interfacial area of the wetting-nonwetting phases and capillary pressure represent M_0–M_2, and that Euler characteristic representing M_3 (the integrated Gaussian curvature) has been ignored in two-phase flow characterization. Supported by a mathematical theorem, it seemed that χ could be the missing piece to fill the knowledge gaps in the study of two-phase flow in porous media. Herring et al. (2015) found that there was a linear relationship between the initial Euler characteristic (χ) of the nonwetting phase and the capillary trapping efficiency.

Avraam and Payatakes (1995) observed a dependency of relative permeabilities on the changes in microscopic flow regimes when the flow regime changed from ganglion dynamics to connected pathway. They believed that the fractional flow theory had to be modified to account for those changes. Tsakiroglou et al. (2015) developed explicit empirical functions of oil and water capillary number for relative permeabilities and water saturation based on 2-D and 3-D steady state relative permeability measurements. This approach

made it possible to emphasize on the effect of the local flow rates on the relative permeabilities and flow regime.

The recent flow experiments by synchrotron X-ray microtomography coupled with modeling has also contributed to improving the traditional theory of the relative permeability (Wyckoff & Botset, 1936). Relative permeability depends on pore scale fluid configuration which in turn, depends on other parameters, one of which could be connectivity (Armstrong et al., 2017). Berg et al. (2016a, 2016b) computed the relative permeabilities by Navier-Stokes equation on the connected pathways of the wetting and nonwetting phases obtained by synchrotron microtomography, and compared the results with the measured ordinary steady state relative permeabilities of the same core material on the Darcy scale. They reported the simulated relative permeabilities were similar to the ordinary ones; but the simulated endpoint saturations were 10% higher than the measured endpoints in the Darcy scale. However, the simulated microtomography and the measured results matched when they were normalized to the mobile saturation range. Armstrong et al. (2017) stated the ganglion dynamics resulted in smaller Corey exponents (Corey, 1954) and larger endpoint relative permeabilities. Overall, recent advances have been promising for better understanding of two-phase flow in porous media.

In this work, we studied the drainage and imbibition by brine and surfactant in a flow experiment in a water-wet Berea sandstone sample. The Euler characteristic (χ) was calculated for both wetting and nonwetting phases. In addition, χ of ganglia and connected pathways of the wetting and nonwetting phases were calculated to understand their topological changes in the two-phase flow. The role of nonwetting ganglia and connected pathway in the flow and their volume exchange were further investigated by calculating the Betti numbers and volumes of these two entities.

2. Materials and Methods

2.1. Material Properties

The core sample was a Berea sandstone ($D = 4$ mm, $L \approx 10$ mm) extracted from a parent plug which had a permeability and porosity of 270 mD and 15.2%, respectively. A single-phase flow simulation by Navier-Stokes equation performed using GeoDict software (version 2017, Math2Market GmbH, Kaiserslautern, Germany) computed permeability of the imaged part of the core. The calculated permeability was 286.3 mD. There was no aging before the experiment and the core sample was strongly water wet. The mineral composition of the rock (mineral wt %) was 92.1 quartz, 0.9 plagioclase, 5.9 alkali feldspar, and 1.1 diopside (Khanamiri et al., 2016a, 2016b).

The composition of the brines is given in Table 1. The core was initially saturated with high salinity water (HSW in Table 1). The ionic strength of low salinity water (LSW) was 10 times lower than that of the HSW. The LSW that contains only NaCl salt is denoted by LSW-N, while LSW that contains both NaCl and $CaCl_2$ salts is denoted by LSW-NC. The low salinity surfactant (LSS) solutions were prepared by dissolving 0.5 wt % surfactant in the LSW-N and LSW-NC. The corresponding surfactant solutions of the LSW-N and LSW-NC are denoted by LSS-N and LSS-NC, respectively. The surfactant is a blend of alkylbenzene sulfonates with a chain length distribution of C_{15}-C_{18} (Khanamiri et al., 2016a, 2016b). Details of the surfactant properties are available in the mentioned references.

Table 1
Composition of the Brines and Surfactant Solutions

Brine	NaCl (g/L)	$CaCl_2 \cdot 2H_2O$ (g/L)	$MgCl_2 \cdot 6H_2O$ (g/L)	M^{2+}/M^{+} [a]	Ionic strength (mol/L)
HSW	29.250	2.210	0.305	0.033	0.5561
LSW-N	3.25			0	0.0556
LSW-NC	3.202	0.0404		0.005	0.0556
LSS-N	0.5 wt % surfactant dissolved in LSW-N				
LSS-NC	0.5 wt % surfactant dissolved in LSW-NC				

Note. M^{2+}/M^{+} is the molar ratio of divalent to monovalent cations.

Table 2
Details of Injection and Image Acquisition

Injection step	Injection	Flow rate (mL/min)	Capillary number[a]	Duration (≈min)	PVI[b]	PVI-FOV[c]	PVI-FOV per scan[d]	Scan number
1	Oil injection 1	0.004	2.0×10^{-5}	35	7	21	1.2	1–18
2	Oil injection 2	0.04	2.0×10^{-4}	10	20	60	12	19–23
3	HSW1	0.004	1.0×10^{-6}	15	3	9	1.2	24–31
4	HSW2	0.008	2.0×10^{-6}	15	6	18	2.4	32–39
5	LSS1-NC	0.008	3.5×10^{-4}	20	8	24	2.4	40–49
6	LSS2-N	0.008	1.1×10^{-4}	20	8	24	2.4	50–58
7	LSS3-NC	0.008	3.5×10^{-4}	20	8	24	2.4	59–69
8	LSS4-N	0.008	1.1×10^{-4}	20	8	24	2.4	70–81

[a]Capillary number equals μv/IFT, where μ and v are the viscosity and velocity of the injected fluid, respectively, and IFT is the interfacial tension between the injected and displaced fluids. [b]PVI was the injected volume in terms of number of the pore volume of the whole core. The pore volume of the core with 10 mm length was roughly 0.02 mL. [c]PVI-FOV is the PVI for the field of view (FOV) of imaging. [d]PVI-FOV per scan is the number of PVI-FOV injected into the FOV every 2 min, which is the duration of one scan.

The nonwetting phase used in the flow experiment was a mixture of 90% by volume crude oil and 10% 1-Idododecane. 1-Idododecane enhances the contrast of the nonwetting and wetting phases. The crude oil had a density of 0.8582 g/cm^3 and a viscosity of 19.90 mPa s, both measured at 15°C (Tichelkamp et al., 2014). Interfacial tension (IFT) of the nonwetting phase with the HSW, LSS-N, and LSS-NC were 5.3, 0.1, and 0.03 mN/m, respectively, at room temperature.

2.2. Injection and Imaging

The experiment was conducted at ambient conditions in the TOMCAT beamline at the *Swiss Light Source, Paul Scherrer Institute*. A schematic diagram of the experimental setup is shown in supporting information Figure S1 under *Method* section (*S1, flow system*). Description of the schematic diagram is also available in the same section. Details of the injection steps are listed in Table 2. The core sample was 100% saturated with HSW (Table 1) before starting the experiment. The drainage started at $S_w = 1$, while the image acquisition started slightly later due to experimental limitations. The first recorded saturation is therefore 0.75. Drainage was performed at two different flow rates. Waterflooding was done by HSW at two different flow rates. Low salinity surfactant (LSS) was then injected in four different steps denoted by LSS1-NC, LSS2-N, LSS3-NC, and LSS4-N. LSS-N is the LSS with NaCl only and the LSS-NC is the one with both NaCl and $CaCl_2$ (see Table 1).

The X-ray microtomography was performed during the injections. Image acquisition in each scan took roughly 18 s and the time interval between two scans was approximately 2 min. The rest of the 2 min period was used by the machine to reposition the rotation stage and to prepare for the next scan. Nine hundred projections were taken in a 180 degree rotation (0.2 degree angular step) with 20 ms exposure time in each angular step. The beam energy was 21.9 keV. The isotropic pixel size of the projections was 3.25 μm and the vertical field of view (FOV) for camera was 2,866 μm. This is roughly 1/3rd of the total core length. 2,447 μm of the FOV was analyzed. The number of scans per injection step is shown in the last column of Table 2. Details of image analysis are available in supporting information under *Method* section (S1, Image processing).

Details of the methodology are available in supporting information (Doube et al., 2010; Kanungo et al., 2002; Khanamiri et al., 2016b; Münch, 2015; Nock & Nielsen, 2004; Otsu, 1979; Perona & Malik, 1990; Rasband, 1997–2016; Ridler & Calvard, 1978; Tschmperlé & Deriche, 2005).

3. Results and Discussion

In this work, oil was the nonwetting phase and water was the wetting phase. The largest oil cluster was assumed the oil connected pathway and the rest of the clusters were assumed to be the oil ganglia. It is discussed later that these two entities have volume exchange during the injections. The same assumption was made for the water phase. The total phase is therefore the summation of the connected pathway and

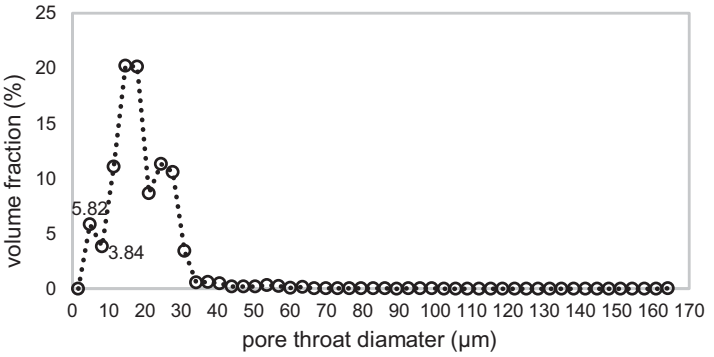

Figure 1. Pore throat size.

ganglia. The Euler characteristic of the total oil phase, oil ganglia, and oil connected pathway is symbolized by χ_{oT}, χ_{oG}, and χ_{oP}, respectively. The Euler characteristic of the total water phase, water ganglia, and water connected pathway is denoted by χ_{wT}, χ_{wG}, and χ_{wP}, respectively. Further, the Betti numbers (β_0 and β_1) and volumes of the ganglia and connected pathway of the nonwetting phase were also investigated to study both their exchange and topological behavior. In addition, common interfacial area of the wetting and nonwetting phase is presented and discussed. We normalize Euler characteristics, Betti numbers, and interfacial area by dividing the values by the bulk volume of the system, which is 26 mm^3.

The injection experiment involved several steps of oil, water, and surfactant injections. The order of the injection steps in the experiment was listed in Table 2. The numbers for the injection steps (1–8) were also shown on the figures where the horizontal axes were time and scan numbers. The next section addresses the experimental limitations that might have affected the results.

3.1. Experimental Limitations

It is believed that the wetting phase is continuous while the results suggest otherwise, mainly due to the limited spatial resolution. Thus, the presented results for the wetting phase could be influenced by the limitation in detecting submicron wetting films. However, we decided to present the results of the wetting phase, because the contribution of the submicron films to flow may be negligible due to the insignificant hydraulic conductivity.

The temporal resolution of 2 min might not be enough to capture the dynamics at the injection transition. The changes of different parameters shortly after the injection switches are expected to be larger compared to the late time changes when the effect of new injection is likely alleviated. In Table 2, the column PVI-FOV per scan represents the volume of injected fluids every 2 min. All the values are above one pore volume, i.e., the first scan after the switch represents the state of the system at which more than one pore volume of new fluid is injected. Therefore, a part of the transient behavior was not imaged. This explains the sudden jumps for some of the calculated parameters at the injection transitions.

GeoDict package was utilized to calculate the pore throat size (see Figure 1). The mean throat diameter was roughly between 15 and 18 μm, while the spatial resolution was 3.25 μm. About 5.8% of the pores have a throat diameter at the interval of 3.25–6.5 μm. A part of these small constrictions, which are often filled with water, are likely removed in image processing. However, there is no available experimental evidence to check the extent of possible changes. Nevertheless, influence of those changes on the results might not be as significant as the mentioned effect of spatial resolution on the wetting phase connectivity.

Further, the number of flow paths in contact with the upper and lower boundaries of the imaging field of view is roughly 300 in each side. On the other hand, the number of oil clusters inside the field of view throughout the experiment is roughly in the order of 20,000–30,000 (see section 3.6). Therefore, in case some of the clusters of the oil ganglia form a connection with the connected pathway outside the field of view, the associated error on the calculated Euler characteristic of the nonwetting phase (oil), volumes of the connected pathway and ganglia, and the Betti numbers could be negligible.

3.2. Effect of Injection Rate on χ of Nonwetting Phase

As shown in Figure 2, Euler characteristic of the total oil phase (χ_{oT}) reduces in drainage when the volume of the oil phase increases. However, χ_{oT} increases sharply by a 10-fold increase in the injection rate during drainage. Afterward, χ_{oT} starts to reduce again as the water saturation reduces further. The imbibition starts by HSW injection with low injection rate followed by HSW with double rate. χ_{oT} increases while water imbibes into the core. However, it does not represent a sharp change by the injection rate increase. The large drop in connectivity of the oil phase after the rate increase during drainage might have been caused by the large increase in the number of oil clusters. This is explained later in the context of Betti numbers.

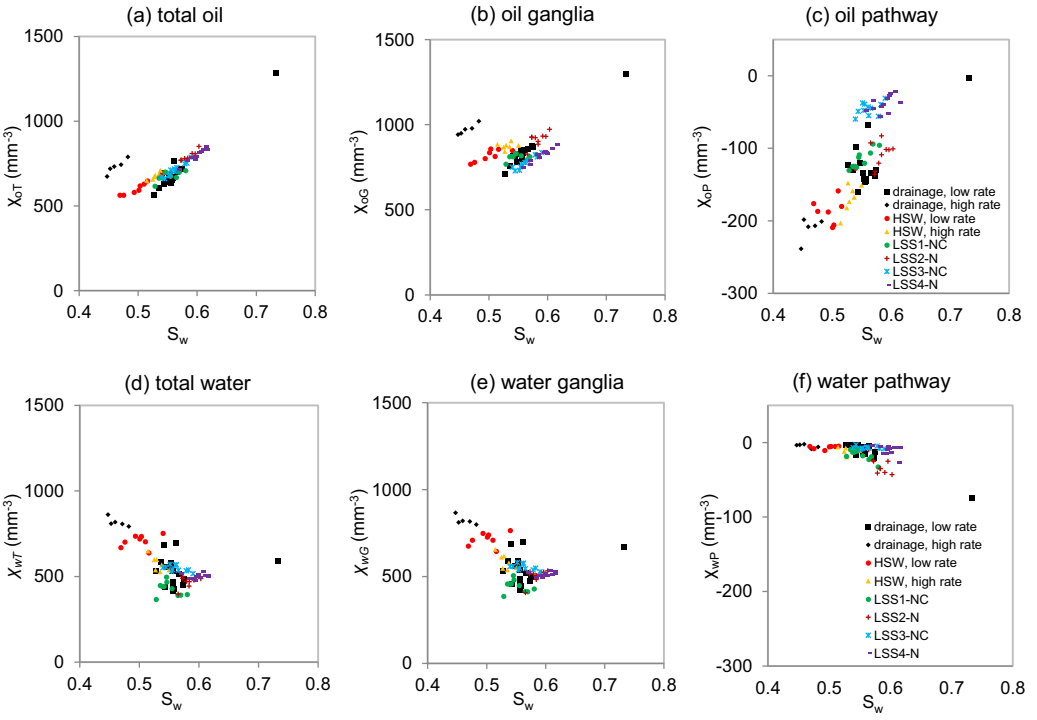

Figure 2. Euler characteristic (χ) of (a) total oil phase—ganglia plus connected pathway, (b) oil ganglia, (c) oil connected pathway, (d) total water phase, (e) water ganglia, and (f) water connected pathway in drainage and imbibition.

3.3. Hysteresis in $\chi - S_w$ in Imbibition and Drainage

The Euler characteristic of the total oil phase (χ_{oT}) versus S_w at high salinity water (HSW) injection is different from that at drainage, as shown in Figure 2. Therefore, χ_{oT} represents a hysteresis behavior between drainage and imbibition. The χ for the oil pathway and ganglia was calculated to investigate the hysteresis in topology of these entities (see Figure 2). As shown in Figure 2, hysteresis is apparent in χ_{oG} of the oil ganglia versus water saturation. χ_{oG} is similar to χ_{oT}. However, the connected pathway does not show hysteresis in drainage and imbibition. In the case of the wetting phase (water), χ_{wG} and χ_{wT} are also similar (see Figure 2). Although the data are slightly more scattered, it seems that there is also a hysteresis in χ_w between drainage and imbibition for the water ganglia (χ_{wG}) and the total water phase (χ_{wT}). Similar to the oil connected pathway, the water connected pathway has nearly no hysteresis in drainage and imbibition.

According to equation (1), Euler characteristic (χ) determines the topology by summing up the changes in the number of clusters (β_0, zeroth Betti number), number of redundant connections (β_1, first Betti number) and number of cavities (β_2, second Betti number). χ has been the main parameter in studying the topology of the fluid phases in the recent works. Examples have been mentioned in section 1. However, in order to study the interactions between ganglia and connected pathway and to learn about their contribution in fluid phase topology, we present also the Betti numbers and the volumes of ganglia and connected pathway in the next section.

3.4. Betti Numbers

Ganglia and connected pathway are dependent entities. If a cluster from ganglia merges with connected pathway, it is not a part of ganglia anymore. It will be counted as a part of connected pathway. Alternatively, if a droplet separates from connected pathway, it will be counted as a part of ganglia. There can be an exchange between ganglia and connected pathway. The Betti numbers and the volumes of the ganglia and connected pathway are capable of showing the interchange between ganglia and connected pathway. The calculations showed that the second Betti number (β_2) or the number of cavities is negligible compared to β_0 and β_1. In addition, β_0 of the connected pathway is one, i.e., β_0 and β_1 of the ganglia and β_1 of the connected pathway are the main Betti numbers contribute in the topology of a phase. Moreover,

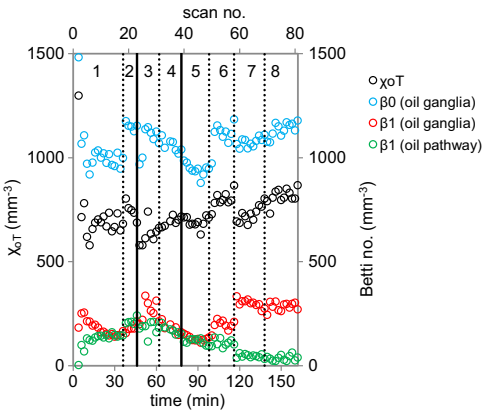

Figure 3. β_0 (number of clusters) and β_1 (number of redundant connections) of the oil ganglia, β_1 of the oil connected pathway and χ for the oil phase versus time and scan number at injection steps 1–8 (see Table 2).

summation of χ of the ganglia and connected pathway equals the χ of the total phase because χ is an *additive* property. Therefore, with a good accuracy, Euler characteristic (equation (1)) can be simplified as follows:

$$\chi=\chi_G+\chi_P=(\beta_0-\beta_1+\beta_2)_G+(\beta_0-\beta_1+\beta_2)_P=\beta_{0G}-\beta_{1G}-\beta_{1P} \quad (2)$$

Subscripts *G* and *P* stand for ganglia and pathway, respectively. Figure 3 shows β_0 and β_1 of the ganglia, β_1 of the connected pathway and χ of the nonwetting (oil) phase. This reveals the nature of ganglia and connected pathway contributions on the topological changes. In addition, Figure 4 shows the volume of the connected pathway and ganglia for the oil phase. Figures 3 and 4 help distinguishing whether the topology change is because of exchange between ganglia and pathway or from internal changes of the ganglia clusters and connected pathway. Below, this has been investigated in different injection steps throughout the experiment.

In drainage (injection step 1), the volume of oil ganglia is large compared to that of the oil connected pathway. The volume and β_1 of oil pathway keep increasing while the volume and β_1 of oil ganglia decreases. Simultaneously, the number of ganglia reduces slightly. These suggest that some clusters separate from oil ganglia (reduction in ganglia β_0 and β_1) and merge with oil connected pathway (increase in pathway volume and β_1). In step 2 of drainage where the flow rate increases by 10-fold, the number of ganglia (β_0) increases dramatically right after rate increase while β_1 of both oil ganglia and pathway increase only slightly. The rate change increases total oil volume (see S_w reduction in Figure 4b). Both ganglia and connected pathway have gained volume by the rate increase (Figure 4a). Furthermore, snap-off is known as a mechanism for trapping of nonwetting phase during imbibition (Singh et al., 2017a). The high number of ganglia (β_0) at high flow rate drainage (step 2) implies the occurrence of "snap-off during drainage" which is not well understood. Possible occurrence of snap-off suggests that a number of the ganglia clusters could be isolated. Example 3-D images of the nonwetting ganglia and connected pathway at the drainage with low late are presented in supporting information (Figure S5).

In low rate water injection (step 3), β_1 of ganglia first increases sharply then reduces while β_0 of ganglia and β_1 of connected pathway reduce nearly in the whole interval, i.e., some of the clusters in ganglia likely merge with each other. The reduction in all three Betti numbers happens while the volumes of both entities reduce. Considering the increase in water saturation (see Figure 4b), it is likely that both entities contribute to saturation change with little or no volume exchange between them. High rate water injection (step 4) starts with increase in volume of connected pathway and reduction in ganglia volume. This is a sign of

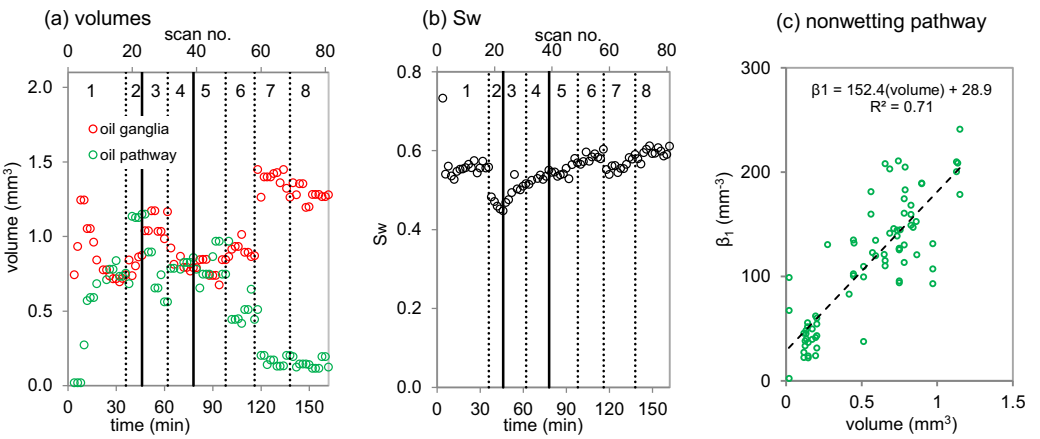

Figure 4. (a) Volume of ganglia and connected pathway for oil phase, and (b) water saturation versus time and scan number at injection steps 1–8 (see Table 2); (c) β_1 (number of redundant connections) versus volume of the nonwetting connected pathway.

exchange between ganglia and connected pathway. All three Betti numbers are reducing in this step similar to step 3. In steps 3 and 4, total contribution of reduction in β_1 of both oil ganglia and oil connected pathway in total topology change is stronger than contribution of the reduction in β_0, because, as Figure 3 shows; χ_{oT} increases in this period.

In first surfactant injection (step 5), volume of oil ganglia decreases, volume of oil connected pathway increases, but not monotonically, and number of oil clusters in ganglia (β_0) reduces. These points imply that there is an exchange between ganglia and connected pathway. Upon switching to the second surfactant injection (step 6), volume of oil ganglia rises while volume of oil connected pathway drops and the water saturation (Figure 4b) increases, i.e., connected pathway is responsible for both oil production and increase in the ganglia volume. The switch from step 5 to step 6 causes also an increase in β_0 and β_1 of the ganglia.

Injected fluids in steps 7 and 8 are the same as those in steps 5 and 6, respectively. Saturation history in steps 7 and 8 is similar to that in steps 5 and 6 (see Figure 4b), most likely caused by an oil invasion into the field of view of the imaging camera. The similarity in saturation history is discussed later. The changes in volume and connectivity of nonwetting ganglia and connected pathway at the transition from injection 6 to 7 seem to be considerable. As presented in Table 2, the injected PV per scan for the field of view (FOV) at surfactant injections is 2.4. Therefore, the changes between the last data point in stage 6 and the first one in stage 7 represent the effect of 2.4 PV injection. This injected volume contains both surfactant and oil. The outcome might be combined effect of several phenomena, which are not distinguishable in the presented experiment. There are two major phenomena; one is increase in volume and connectivity of the nonwetting ganglia in the period invaded oil and surfactant have been injected into the FOV. This could mean that the injected oil has partly joined the ganglia increasing connectivity and volume of ganglia. Simultaneously, the volume and connectivity of nonwetting pathway have both decreased, i.e., the pathway is either contributing to oil production or to increase in volume and connectivity of ganglia. The mentioned changes for nonwetting phase particularly for the nonwetting pathway might be a sing of wetting change after injection of surfactants with different ionic compositions.

Overall, Figure 4a indicates that the volume of oil ganglia is a considerable part of the total oil volume. In addition, Figure 3 shows that β_1 of the ganglia is also comparable to β_1 of the connected pathway. These two points reveal that the ganglia contains redundant pathways and contributes to the flow by creating redundant connections and by constituting a part of the phase volume. β_0 of the ganglia plays also a major role in total topology (see Figure 3). It should be emphasized that the topological changes in nonwetting ganglia can also result in topological changes in the wetting phase. The other major result is that the number of redundant connections (β_1) in oil connected pathway versus time has a general tendency to increase in drainage and to decrease in imbibition both with relatively smooth profiles, with little sensitivity to the

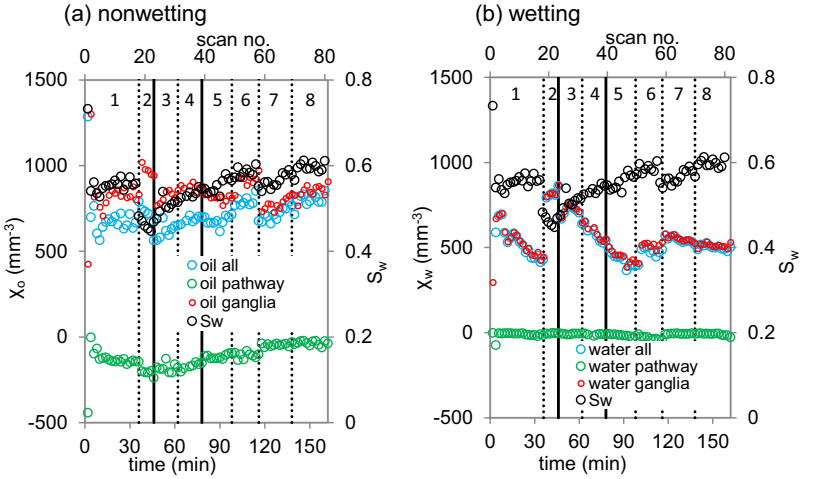

Figure 5. Evolution of χ for (a) nonwetting and (b) wetting phases for the whole phase (all), ganglia and connected pathway; χ (*left vertical axis*) is shown by red, green, and blue circles. S_w (*right vertical axis*) is shown by black circles. The numbers 1–8 represent the injection steps mentioned in Table 2.

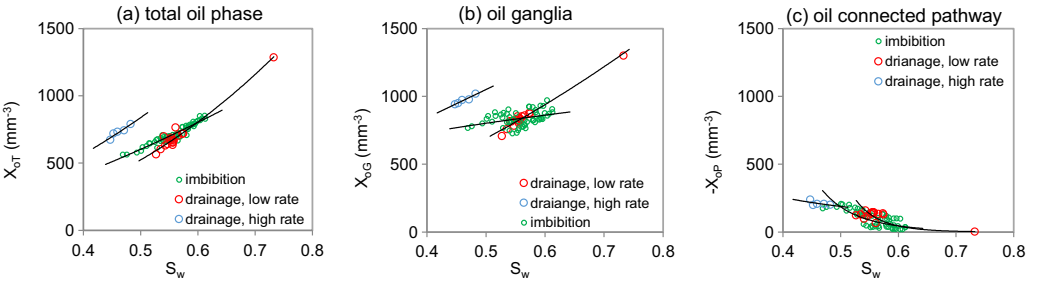

Figure 6. χ_o of the (a) oil phase, (b) oil ganglia, and (c) oil connected pathway versus S_w in drainage (separate low and high rates) and imbibition. The curves are the power law fit on the experimental data. The sign of χ_{oP} is changed to positive to fit the power law curves. Exponents and correlation coefficients (r^2) are presented in Table 3.

changes of rate or IFT throughout the experiment. Further, Figure 4c shows that β_1 versus volume for the oil connected pathway has a relatively linear trend.

3.5. Reproducibility of χ Versus Time

Changes of Euler characteristic versus time shows that the difference between χ_{wG} and χ_{wT} is insignificant while there is a slight difference between χ_{oG} and χ_{oT} (Figure 5). The connected pathway of oil becomes closer to the threshold of major fragmentation ($\chi_{oP} \approx 0$) at the start of injection step 7 (third surfactant injection) and continues flowing under similar condition in steps 7 and 8; simultaneously, χ_{oG} approaches χ_{oT}.

There is a reduction in S_w at injection step 7 (LSS3-NC), due to oil invasion from upstream of field of view of camera. S_w in step 7 is similar to that in step 5 (see Figure 5). S_w profiles of steps 6 and 8 are also similar. Therefore, the oil invasion made it possible to observe the changes in topology when the S_w history was repeated in surfactant injection. Figure 5 shows that χ_{oT} (oil phase) is nearly reproducible in the mentioned injection steps while χ_{oG} (oil ganglia) has minor similarity in these two periods. On the other hand, χ_{wT} values and trend in steps 7 and 8 are different from those in steps 5 and 6. χ_{wG} exhibited similar behavior. In case of the connected pathways, χ versus time is not reproducible before and after invasion of upstream oil in none of the water and oil phases.

Schlüter et al. (2016) believed that changes of the nonwetting phase Euler characteristic with changing saturation was process-dependent, i.e., drainage and imbibition had different $\chi_o - S_w$ curves. As discussed earlier and shown in Figure 2, we observed also the same hysteresis behavior for the nonwetting phase in imbibition and drainage. This implies that possible correlations between Euler characteristic and saturation, if there is any, is likely different in drainage and imbibition. Here we investigate the correlation of the nonwetting phase χ with S_w in imbibition and drainage (see Figure 6a). The drainage includes two steps with a 10-fold difference in the injection rate, which resulted in large difference in χ versus S_w. Therefore, we correlate χ with S_w separately for these two steps. In addition, the $\chi_o - S_w$ correlations for the oil ganglia and

Table 3
Power Law Exponents and Correlation Coefficients of χ_o Versus S_w for the Total Oil Phase, Oil Ganglia and Connected Pathway in Different Processes

	Process	Exponent	r^2	Number of data points
Total oil phase	Drainage, low rate	2.36	0.934	18
	Drainage, high rate	1.76	0.878	5
	Imbibition	1.57	0.918	58
Oil ganglia	Drainage, low rate	1.69	0.956	18
	Drainage, high rate	0.99	0.935	5
	Imbibition	0.39	0.144	58
Oil connected pathway[a]	Drainage, low rate	−12.59	0.859	18
	Drainage, high rate	−1.35	0.313	5
	Imbibition	−7.70	0.509	58

[a]The sign of χ_{oP} values was changed to positive to obtain a power law fit.

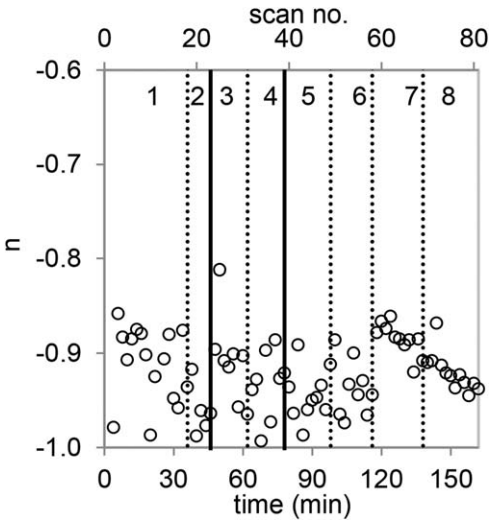

Figure 7. Power law exponents for the nonwetting ganglia size distribution at injection steps 1–8 (see Table 2).

connected pathway were also investigated (see Figures 6b and 6c). Curves generated with power law equation $\chi_o = bS_w^a$ is fitted on the experimental data, and the exponent a is found. The curve fitting resulted in a high correlation coefficient for the total oil phase in the three mentioned processes. Figure 6 shows the fitted curves and the experimental data points. The corresponding exponents and correlation coefficients (r^2) are given in Table 3. Connected pathway of the oil phase represents a good match only for the drainage with low injection rate; while the oil ganglia exhibits a poor correlation in the imbibition, but good correlations in the two drainage processes.

This section concludes that repeating the saturation history (S_w versus time) in surfactant injection reproduced χ_{oT} versus time while the other Euler characteristics were not reproduced. Moreover, a power law fitting equation exhibited a good match for χ_{oT} versus S_w changes when fitted separately on the $\chi_{oT} - S_w$ data of imbibition and drainage with low and high rates. The latter suggests that χ_{oT} which reflects the outcome of all topological changes for the nonwetting phase scales with saturation in all three processes while χ_{oP} and χ_{oG}, which represent only a part of the topological changes for the nonwetting phase, scale with saturation only at some of the processes.

3.6. Ganglia Cluster Size Distribution

Histograms for the volume of the nonwetting ganglia clusters were constructed (see supporting information section S2 and Figure S6). All the curves at different time steps follow a power law with correlation coefficients close to unity. The smallest correlation coefficient was 0.935. Considering N and V as the number and volume of the oil ganglia clusters, respectively; exponent (n) in $N = N_0V^n$ for every time step in the experiment is calculated (see Figure 7). N_0 is a fitting parameter. Values of the exponents are scattered between -1.00 and -0.81 during injection steps 1–6. However, they reduce neatly in steps 7 and 8. It is interesting that, in these two injection steps, χ_{oP} approaches zero, i.e., major fragmentation occurs in the connected pathway of the nonwetting phase (see Figure 5).

Figure 8 shows the variations in the number of oil ganglia clusters, regardless of their volume, in addition to the variations of χ for the oil and water phases. The number of ganglia is the same as β_0 which was discussed in section 3.4. Both χ_{wT} and the number of oil clusters represent simultaneously decreasing or increasing profiles in injection steps 1–6 and in particular during steps 3–5. Both parameters decrease during steps 3–5. The reduction in the number of oil clusters could be caused by either coalescence of oil ganglia clusters, volume transfer from ganglia to connected pathway, or contribution of ganglia in oil production and saturation change. Details are discussed in section 3.4 and displayed in Figures 3 and 4. There will be less oil clusters limiting the access of water clusters to available flow paths in all three cases. Therefore, the Euler characteristic of water reduces; in other words, connectivity of the water increases.

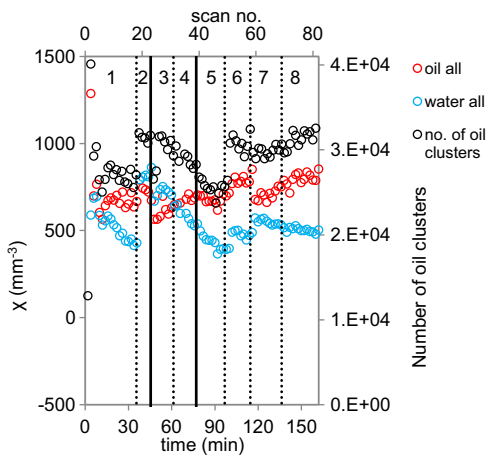

Figure 8. The number of oil clusters (β_0) and χ_{wT} decrease simultaneously or increase simultaneously during injections 1–6.

In this section, we reported that the exponents in the size distribution histograms of the nonwetting ganglia change neatly when the connected pathway is close to major disintegration ($\chi_{oP} \approx 0$). Moreover, the Euler characteristic of the wetting phase and the number of nonwetting clusters decrease or increase simultaneously in most of the injection steps.

3.7. Interfacial Area

Figure 9 shows common interfacial area between water and oil phases (A_{ow}). The values are normalized by bulk volume of the system. The changes in A_{ow} are opposite of the changes in S_w in most of the injection steps, i.e., A_{ow} reduces when the oil volume reduces.

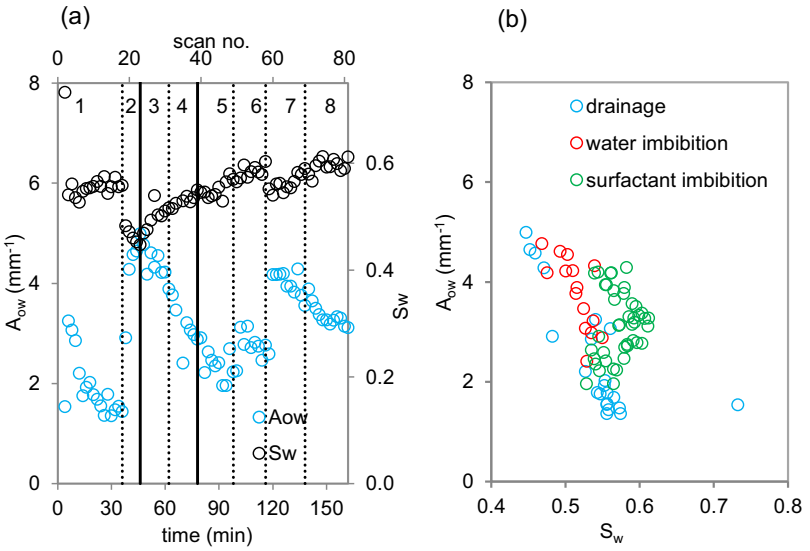

Figure 9. (a) Water/oil interfacial area (A_{ow}) and water saturation (S_w) versus time and scan number, and (b) A_{ow} versus S_w.

Nevertheless, the rate of changes of A_{ow} and S_w is not similar and the two parameters do not correlate (see Figure 9b).

The system normally tends to minimize A_{ow} in order to reach a minimum energy state. However, changes in rate and IFT can sometimes increase A_{ow}. A 10-fold increase in the injection rate in the drainage results in a sharp rise in A_{ow} (Figure 9a). The A_{ow} rise can be explained by increase in the number of clusters in the oil ganglia providing larger contact area with the water phase (see β_0 in Figure 3). In addition, IFT increase associated with switching surfactant injection from step 5 to step 6 increases A_{ow}. β_0 increases in this switch, too. On the other hand, there are also transitions at which the rate increases (step 3 to step 4) or IFT reduces (step 4 to step 5), while A_{ow} reduces. A closer look at β_0 in Figure 3 reveals that the number of oil clusters has a decreasing trend in these cases. Further, the wetting phase saturation increases and the ganglia volume decreases in these transitions (see Figure 4). This might be another reason for the reduction in A_{ow}. Because the reduction in ganglia volume happens by production of ganglia clusters from the system or by coalescence of the ganglia clusters with connected pathway. A_{ow} decreases in both of these cases.

Therefore, the changes in the number of the nonwetting ganglia clusters in the system (β_0), volume of the nonwetting ganglia and the wetting phase saturation can be used to help understand the A_{ow} changes.

4. Conclusions

In a two-phase flow experiment imaged by synchrotron X-ray computed microtomography with the mentioned experimental conditions and limitations, and with further analysis of the ganglia and connected pathway, we learned the following points.

1. Euler characteristic of the nonwetting phase (χ_{oT}) versus wetting phase saturation (S_w) changed dramatically by a 10-fold increase in the injection rate during drainage.
2. The χ_{oT} versus S_w exhibited a hysteresis behavior in drainage and imbibition. Euler characteristic of the ganglia had also hysteresis behavior, while that of the connected pathway had little or no hysteresis in drainage and imbibition.
3. The nonwetting ganglia clusters were capable of contributing to the flow by creating internal redundant connections, volume exchange with connected pathway and saturation change.
4. The number of redundant connections (β_1) in nonwetting connected pathway had an increasing profile in drainage and a decreasing one in imbibition, both with relatively smooth profiles, with negligible sensitivity to the changes in rate and interfacial tension throughout the experiment. Further, β_1 versus volume for the oil connected pathway has a relatively linear trend.

5. Repeating the S_w history (S_w versus time) in surfactant injection reproduced χ_{oT} versus time while the other Euler characteristics were not reproduced. Moreover, a power law fitting equation resulted in a good match for the χ_{oT} versus S_w changes, when fitted separately on the $\chi_{oT} - S_w$ data of imbibition and drainage with low and high injection rates.
6. Furthermore, the major relevance of this work to EOR is that the changes in ionic composition of surfactant solution is capable of changing microscopic flow behavior through modifying the configuration, volume, interfacial area, and connectivity of nonwetting ganglia and connected pathway.

Acknowledgments
The flow experiment and X-ray computed microtomography were performed at the TOMCAT beamline in the Swiss Light Source, *Paul Scherrer*. The authors would like to thank Georg Voss for his help in the preparation and performing the experiment. Morten Vassvik and Reidun Cecilie Aadland are appreciated for their help in performing the experiment. We thank also Per Arne Slotte and Carl Fredrik Berg for the discussions. This work was partly supported by the Research Council of Norway through *Centers of Excellence* funding scheme, project 262644. The tomography images are available at http://doi.org/10.5281/zenodo.1098180.

References

Armstrong, R. T., Georgiadis, A., Ott, H., Klemin, D., & Berg, S. (2014). Critical capillary number: Desaturation studied with fast X-ray computed microtomography. *Geophysical Research Letters*, *41*, 55–50. https://doi.org/10.1002/2013GL058075

Armstrong, R. T., McClure, J. E., Berrill, M. A., Rücker, M., Schlüter, S., & Berg, S. (2016). Beyond Darcy's law: The role of phase topology and ganglion dynamics for two-fluid flow. *Physical Review E*, *94*, 043113. https://doi.org/10.1103/PhysRevE.94.043113

Armstrong, R. T., McClure, J. E., Berrill, M. A., Rücker, M., Schlüter, S., & Berg, S. (2017). Flow regimes during immiscible displacement. *Petrophysics*, *58*(1), 10–18.

Avraam, D. G., Kolonis, G. B., Roumeliotis, T. C., Constantinides, G. N., & Payatakes, A. C. (1994). Steady-state two-phase flow through planar and nonplanar model porous media. *Transport in Porous Media*, *16*, 75–101. https://doi.org/10.1007/BF01059777

Avraam, D. G., & Payatakes, A. C. (1995). Flow regimes and relative permeabilities during steady-state two-phase flow in porous media. *Journal of Fluid Mechanics*, *293*, 207–236. https://doi.org/10.1017/S0022112095001698

Berg, S., Armstrong, R. T., Georgiadis, A., Ott, H., Schwing, A., Neiteler, R., et al. (2015), Onset of oil mobilization and nonwetting-phase cluster-size distribution. *Petrophysics*, *56*(1), 15–22.

Berg, S., Rücker, M., Ott, H., Georgiadis, A., van der Linde, H., Enzmann, F., et al. (2016a). Connected pathway relative permeability from pore-scale imaging of imbibition. *Advances in Water Resources*, *90*, 24–35. https://doi.org/10.1016/j.advwatres.2016.01.010

Berg, S., Rücker, M., Ott, H., Georgiadis, A., van der Linde, H., Enzmann, F., et al. (2016b). Modelling of imbibition relative permeability by direct quasi-static approach. In *International symposium of the society of core analysts, SCA2016-007*, *Colorado*, USA. Houston, TX: Society of Petrophysics and Well Log Analysts (SPWLA). Retrieved from https://www.spwla.org/

Blunt, M. J., Bijeljic, B., Dong, H., Gharbi, O., Iglauer, S., Mostaghimi, P., et al. (2013). Pore-scale imaging and modelling. *Advances in Water Resources*, *51*, 197–216. https://doi.org/10.1016/j.advwatres.2012.03.003

Brown, G. O. (2002). Henry Darcy and the making of a law. *Water Resources Research*, *38*(7), 1106. https://doi.org/10.1029/2001WR000727

Corey, A. T. (1954). The interrelation between gas and oil relative permeabilities. *Producers Monthly*, *19*, 38–41.

Darcy, H. (1856). *Les Fontaines Publiques de la Ville de Dijon*. Paris, France: Dalmont.

Doube, M., Kłosowski, M. M., Arganda-Carreras, I., Cordeliéres, F., Dougherty, R. P., Jackson, J., et al. (2010). BoneJ: Free and extensible bone image analysis in ImageJ. *Bone*, *47*, 1076–1079. https://doi.org/10.1016/j.bone.2010.08.023

Hadwiger, H. (1957). *Vorlesungen über Inhalt, Oberfläche und Isoperimetrie (Lecture on Content, Surface and Isoperimetry)* (312 pp.). Berlin, Heidelberg: Springer.

Haines, W. B. (1930). Studies in the physical properties of soil. V. The hysteresis effect in capillary properties, and the modes of moisture distribution associated therewith. *Journal of Agricultural Science*, *20*, 97–116. https://doi.org/10.1017/S002185960008864X

Herring, A. L., Andersson, L., Schlüter, S., Sheppard, A., & Wildenschild, D. (2015). Efficiently engineering pore-scale processes: The role of force dominance and topology during nonwetting phase trapping in porous media. *Advances in Water Resources*, *79*, 91–102. https://doi.org/10.1016/j.advwatres.2015.02.005

Herring, A. L., Harper, E. J., Andersson, L., Sheppard, A., Bay, B. K., & Wildenschild, D. (2013). Effect of fluid topology on residual nonwetting phase trapping: Implications for geologic CO_2 sequestration. *Advances in Water Resources*, *62*, 47–58. https://doi.org/10.1016/j.advwatres.2013.09.015

Kanungo, T., Mount, D. M., Netanyahu, N. S., Piatko, C. D., Silverman, R., & Wu, A. Y. (2002). An efficient K-means clustering algorithm: Analysis and implementation. *IEEE Transactions on Pattern Analysis and Machine Intelligence*, *24*(7), 881–892.

Khanamiri, H. H., Nourani, M., Tichelkamp, T., Stensen, J. Å., Øye, G., & Torsæter, O. (2016a). Low salinity surfactant EOR with a new surfactant blend: Effect of calcium cations. *Energy & Fuels*, *30*(2), 984–991. https://doi.org/10.1021/acs.energyfuels.5b02848

Khanamiri, H. H., Torsæter, O., & Stensen, J. Å. (2016b). Effect of calcium in pore scale oil trapping by low-salinity water and surfactant enhanced oil recovery at strongly water-wet conditions: In situ imaging by X-ray microtomography. *Energy & Fuels*, *30*(10), 8114–8124. https://doi.org/10.1021/acs.energyfuels.6b01236

Leu, L., Berg, S., Enzmann, F., Armstrong, R. T., & Kersten, M. (2014). Fast X-ray micro-tomography of multiphase flow in Berea sandstone: A sensitivity study on image processing. *Transport in Porous Media*, *105*, 451–469. https://doi.org/10.1007/s11242-014-0378-4

Mecke, K., & Arns, C. H. (2005). Fluids in porous media: A morphometric approach. *Journal of Physics: Condensed Matter*, *17*(9), S503.

Münch, B. (2015). *ImageJ*. Bethesda, MD: U.S. National Institutes of Health, Retrieved from http://imagej.net/Xlib

Nock, R., & Nielsen, F. (2004). Statistical region merging. *IEEE Transactions on Pattern Analysis and Machine Intelligence*, *26*(11), 1452–1458.

Otsu, N. (1979). A threshold selection method from gray-level histograms. *IEEE Transactions on Systems, Man, and Cybernetics*, *9*(1), 62–66. https://doi.org/10.1109/TSMC.1979.4310076

Pak, T., Butler, I. B., Geiger, S., van Dijke, M. I. J., & Sorbie, K. S. (2015). Droplet fragmentation: 3D imaging of a previously unidentified pore-scale process during multiphase flow in porous media. *Proceedings of the National Academy of Sciences of the United States of America*, *112*(7), 1947–1952. https://doi.org/10.1073/pnas.1420202112

Perona, P., & Malik, J. (1990). Scale-space and edge-detection using anisotropic diffusion. *IEEE Transactions on Pattern Analysis and Machine Intelligence*, *12*(7), 629–639.

Rasband, W. S. (1997–2016). *ImageJ*. Bethesda, MD: U.S. National Institutes of Health. Retrieved from https://imagej.nih.gov/ij/

Ridler, T. W., & Calvard, S. (1978). Picture thresholding using an iterative selection method. *IEEE Transactions on Systems, Man and Cybernetics*, *8*, 630–632.

Rücker, M., Berg, S., Armstrong, R. T., Georgiadis, A., Ott, H., Schwing, A., et al. (2015). From connected pathway flow to ganglion dynamics. *Geophysical Research Letters*, *42*, 3888–3894. https://doi.org/10.1002/2015GL064007

Schlüter, S., Berg, S., Rücker, M., Armstrong, R. T., Vogel, H.-J., Hilfer, R., et al. (2016). Pore-scale displacement mechanisms as a source of hysteresis for two-phase flow in porous media. *Water Resources Research*, *52*(3), 2194–2205. https://doi.org/10.1002/2015WR018254

Singh, K., Menke, H., Andrew, M., Lin, Q., Rau, C., Blunt, M. J., et al. (2017a). Dynamics of snap-off and pore-filling events during two-phase fluid flow in permeable media. *Scientific Reports*, *7*(1), 5192. https://doi.org/10.1038/s41598-017-05204-4

Singh, K., Scholl, H., Brinkmann, M., Michiel, M. D., Scheel, M., Herminghaus, S., et al. (2017b). The role of local instabilities in fluid invasion into permeable media. *Scientific Reports*, *7*(1), 444. https://doi.org/10.1038/s41598-017-00191-y

Tichelkamp, T., Vu, Y., Nourani, M., & Øye, G. (2014). Interfacial tension between low salinity solutions of sulfonate surfactants and crude and model oils. *Energy & Fuels*, *28*, 2408–2414. https://doi.org/10.1021/ef4024959

Tsakiroglou, C., Aggelopoulos, C., Terzi, K., Avraam, D., & Valavanides, M. (2015). Steady-state two-phase relative permeability functions of porous media: A revisit. *International Journal of Multiphase Flow*, *73*, 34–42. https://doi.org/10.1016/j.ijmultiphaseflow.2015.03.001

Tschmperlé, D., & Deriche, R. (2005). Vector-valued image regularization with PDE's: A common framework for different applications. *IEEE Transactions on Pattern Analysis and Machine Intelligence*, *27*(4), 506–517.

Wyckoff, R. D., & Botset, H. G. (1936). The flow of gas-liquid mixtures through unconsolidated sands. *Journal of Applied Physics*, *7*(9), 325. https://doi.org/10.1063/1.1745402

Youssef, S., Rosenberg, E., Deschamps, H., Oughanem, R., Maire, E., & Moks, R. (2014). Oil ganglia dynamics in natural porous media during surfactant flooding captured by ultra-fast x-ray microtomography. In *International symposium of the society of core analysts*, *SCA2014-23, Avignon, France*. Houston, TX: Society of Petrophysics and Well Log Analysts (SPWLA). Retrieved from https://www.spwla.org/